Research Article

Ultra-high-linearity integrated lithium niobate electro-optic modulators

Hanke Feng,[1,†] Ke Zhang,[1,†] Wenzhao Sun,[1] Yangming Ren,[2,3] Yiwen Zhang,[1] Wenfu Zhang,[2,3] and Cheng Wang[1,*]

[1]Department of Electrical Engineering & State Key Laboratory of Terahertz and Millimeter Waves, City University of Hong Kong, Kowloon, Hong Kong, China
[2]State Key Laboratory of Transient Optics and Photonics, Xi'an Institute of Optics and Precision Mechanics, Chinese Academy of Sciences, Xi'an 710119, China
[3]University of Chinese Academy of Sciences, Beijing 100049, China
*Corresponding author: cwang257@cityu.edu.hk

Integrated lithium niobate (LN) photonics is a promising platform for future chip-scale microwave photonics systems owing to its unique electro-optic properties, low optical loss, and excellent scalability. A key enabler for such systems is a highly linear electro-optic modulator that could faithfully convert analog electrical signals into optical signals. In this work, we demonstrate a monolithic integrated LN modulator with an ultra-high spurious-free dynamic range (SFDR) of 120.04 dB · Hz$^{4/5}$ at 1 GHz, using a ring-assisted Mach–Zehnder interferometer configuration. The excellent synergy between the intrinsically linear electro-optic response of LN and an optimized linearization strategy allows us to fully suppress the cubic terms of third-order intermodulation distortions (IMD3) without active feedback controls, leading to ∼20 dB improvement over previous results in the thin-film LN platform. Our ultra-high-linearity LN modulators could become a core building block for future large-scale functional microwave photonic integrated circuits by further integration with other high-performance components like low-loss delay lines, tunable filters, and phase shifters available on the LN platform.   © 2022 Chinese Laser Press

https://doi.org/10.1364/PRJ.464650

1. INTRODUCTION

Microwave photonics (MWP) is a powerful technology that makes use of optical devices and systems to perform microwave signal generation, manipulation, and transmission tasks. Recent advances in integrated photonics have further propelled the realization of MWP functionalities in compact and cost-effective chip-scale systems, i.e., integrated MWP [1]. Many intriguing MWP applications have been realized in various platforms such as silicon (Si) [2,3], silicon nitride (SiN) [4,5], and indium phosphide (InP) [6,7], including broadband microwave signal generation [2,3], tunable true time delay [5], and programmable MWP filters [6]. At the heart of almost all MWP systems sit the electro-optic (EO) modulators, which are responsible for faithfully encoding signals from the microwave to the optical domain. During this process, modulation linearity, often quantified as the spurious-free dynamic range (SFDR) [8], is the most critical metric that ultimately determines the MWP link performance. A modulator with high SFDR could efficiently transmit analog microwave signals while introducing minimal unwanted spurious harmonics (e.g., third-order intermodulation distortions, IMD3) or noises.

The recently emerged thin-film lithium niobate (LiNbO₃, LN) platform is an excellent candidate for future high-performance integrated MWP systems [9]. The Pockels effect in LN is intrinsically linear and low-loss, ideally suited for realizing high-linearity EO modulators. Even today, the highest SFDRs are still achieved using traditional ion-diffused LN modulators that are bulky and difficult to integrate [10,11]. Compared with these bulk LN counterparts, the thin-film LN platform preserves the excellent material properties of LN, but at the same time provides much better light confinement, integrability, and compactness due to its dramatically increased refractive index contrast [9]. More importantly, the LN platform is now endowed with a full range of high-performance devices, including broadband frequency comb sources [12–15], ultra-high-Q microresonators [16,17], programmable filters [18], and efficient frequency converters/shifters [19–21], as well as low-loss delay lines [22], which could potentially be integrated with high-linearity EO modulators on the same photonic chip for complex MWP functions. To date, many miniaturized and high-performance thin-film LN modulators have been demonstrated, exhibiting ultra-high bandwidths beyond

100 GHz, CMOS-compatible drive voltages, and low optical losses [23–29]. However, these modulators are mostly designed for digital communications only. The measured SFDRs of state-of-the-art integrated LN modulators are only ~100 dB · Hz$^{2/3}$ [24,25], which are far from what the material itself could possibly support, mainly restricted by the sinusoidal transfer function of the Mach–Zehnder interferometers (MZIs). Realizing a high-linearity integrated LN modulator that could exploit the full potential of the LN material will greatly boost the development of LN-based MWP systems.

To compensate for the nonlinear transfer function of a simple MZI, several linearization strategies via the implementation of novel device architectures have been proposed and adopted on various integrated photonic platforms. For example, using the ring-assisted MZI (RAMZI) scheme [30–35], SFDR values up to 111.3 dB · Hz$^{2/3}$ have been demonstrated in Si [33], and 117.5 dB · Hz$^{2/3}$ on an InP/Si heterogeneous platform [34], much higher than those achieved in simple MZI/ring modulators [36,37]. However, both Si and InP modulators rely on intrinsically nonlinear modulation mechanisms, i.e., free-carrier injection [38] and the quantum confined Stark effect [39]. The linearization conditions of these modulators are, therefore, further complicated in order to compensate for the nonlinearities from both the device architecture and the material response. As a result, these RAMZI demonstrations have not been able to exploit the full promise of this linearization strategy—cubic terms of IMD3 cannot be fully suppressed and remain the dominant spurious harmonic species [33–35]. More complicated device configurations, such as dual-series [40] and dual-parallel [41] MZI structures, could be used to achieve the full cancellation of the cubic or even the fifth-order terms of IMD3. However, the high insertion loss and the requirement for complicated active feedback controls make these devices less competitive in practical applications. An ideal EO modulator for analog MWP systems should feature a linear material EO response, a simple linearization strategy (e.g., RAMZI), low optical loss, and high-power handling capability to minimize amplifier-induced system noises, as well as chip-scale compatibility with other functional photonic devices, simultaneously.

Here we demonstrate such an ultra-high-linearity modulator satisfying all the requirements above based on the integrated LN platform. The synergy between the excellent material properties of LN and an optimized RAMZI configuration allows us to demonstrate an ultra-high measured SFDR of 120.04 dB · Hz$^{4/5}$ at 1 GHz by fully suppressing the cubic terms of IMD3. The results are nearly 20 dB higher than our reference MZI modulator as well as previous record in the thin-film LN platform.

2. DEVICE DESIGN AND WORKING PRINCIPLE

Figure 1 shows the full microscope image and working principle of our RAMZI modulator, where a racetrack resonator with a free spectral range (FSR) of 50 GHz is coupled with one path of an MZI. When input analog RF signals containing multiple frequency tones [f_1 and f_2 in our experiment, as shown in Fig. 1(a)] are upconverted into optical frequencies, the nonlinearity in the EO modulation process would induce unwanted

spurious IMD3 components (i.e., $2f_1 - f_2$ and $2f_2 - f_1$) that are close by and could interfere with the signal frequencies [Fig. 1(a)]. For a simple MZI biased at the quadrature point, a linear phase change $\Delta\varphi_{\text{mzi}}$ would be translated into a sub-linear intensity change, i.e., $\frac{1}{2}[1 + \cos(\Delta\varphi_{\text{mzi}} - \frac{\pi}{2})]$, when the two arms combine, leading to a nonlinear transfer function [Fig. 1(c)]. In our RAMZI, as the schematic diagrams in Figs. 1(b)–1(d) illustrate, the modulation phase change $\Delta\varphi_{\text{mod}}$ is applied on the ring/racetrack resonator instead, which operates in the deep overcoupling state and is biased at the off-resonance point. By engineering the coupling coefficient κ with respect to the intrinsic round trip transmission coefficient τ, the phase response of the ring resonator $\Delta\varphi_{\text{ring}}$ could be fine-tuned to achieve a super-linear relationship with the modulation phase $\Delta\varphi_{\text{mod}}$ [red curve in Fig. 1(b)], which could precisely compensate for the sub-linearity of the MZI [Fig. 1(c)] to eliminate the cubic terms of IMD3 [30]. As a result, the output intensity of the RAMZI shows a much-linearized Fano line shape with respect to the modulation phase [Fig. 1(d)].

The IMD3 components in the modulated optical field can be derived by performing Taylor expansion to the transfer function of the RAMZI at the corresponding bias point [42]:

$$
\begin{aligned}
&A_{\text{IMD3}} \cdot \cos[(2f_1 - f_2)t] \\
&= \left\{ \frac{3}{4} V_{\text{RF}}^3 \left[\frac{1}{3!} \frac{d^3 I_{\text{out}}(\kappa)}{dv^3} \right] + \frac{25}{8} V_{\text{RF}}^5 \left[\frac{1}{5!} \frac{d^5 I_{\text{out}}(\kappa)}{dv^5} \right] + \cdots \right\}_{v=V_{\text{bias}}} \\
&\quad \cdot \cos[(2f_1 - f_2)t],
\end{aligned}
\tag{1}
$$

where A_{IMD3} represents the amplitude of the IMD3 components, including all odd-order nonlinearities and initially dominated by the cubic terms, v is the driving two-tone signal, i.e., $v = V_{\text{RF}}[\cos(f_1 t) + \cos(f_2 t)] + V_{\text{bias}}$, V_{RF} denotes the amplitude of the RF signals, V_{bias} is the bias voltage, f_1 and f_2 are two closely separated RF frequencies, κ is the coupling coefficient of the racetrack resonator, and I_{out} is the output optical power. The required coupling coefficient κ could be calculated by eliminating the cubic term of IMD3 [first term in Eq. (1)] at the off-resonance bias point. In this case, the dominant spurious harmonic becomes the fifth-order IMD3 term [second term in Eq. (1)] [30,31].

In our particular device, the racetrack resonator features a total round trip length of 2.74 mm and an intrinsic Q factor of 1.1×10^6 (measured using a reference racetrack resonator fabricated on the same chip), which corresponds to an intrinsic round trip transmission coefficient τ of 0.988. The required coupling coefficient κ is calculated to be 0.96. This strong coupling is achieved by an optimized 2×2 multimode interferometer (MMI), designed using full 3D finite-difference time domain (FDTD) simulations (Ansys Lumerical). The core MMI region has a size of 31.4 μm × 4.8 μm. The widths of the input waveguides are first tapered from 1.2 μm to 2.15 μm over a taper length of 15 μm before entering the MMI region to minimize scattering loss. The output waveguides are tapered in a similar but reversed manner.
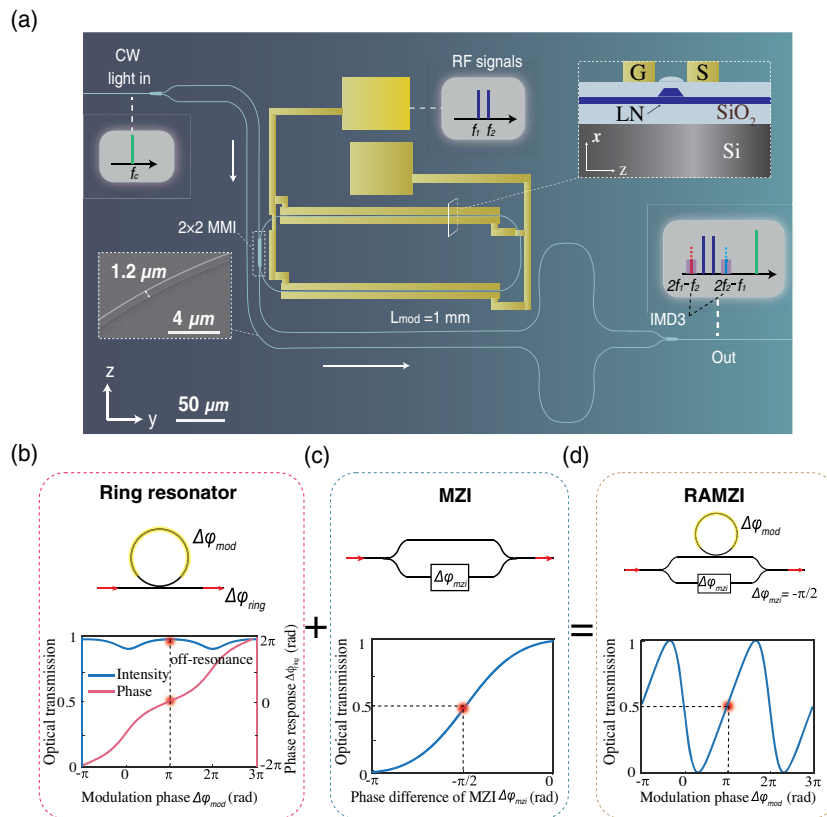
Fig. 1. Schematic of the high-linearity RAMZI modulator. (a) False-color microscope image of the fabricated LN RAMZI modulator, where a racetrack resonator is overcoupled to the top path of an MZI via a 2 × 2 MMI coupler. Two pairs of ground-signal modulation electrodes are placed along the straight arms of the racetrack resonator to induce phase modulation. Two closely spaced RF signals (f_1 and f_2) are upconverted to optical frequencies (near f_c) via the modulator. The RAMZI is designed to provide a linearized EO response and suppress the unwanted spurious harmonics (i.e., $2f_1 - f_2$ and $2f_2 - f_1$) in the output modulated optical signal. The right inset shows the cross section view of the modulation region. The left inset shows the SEM image of the waveguide bend region. (b)–(d) Working principle of the RAMZI modulator. The ring/racetrack resonator in deep overcoupling state functions as an all-pass filter near the off-resonance point (b), where the output phase response $\Delta\varphi_{\mathrm{ring}}$ exhibits a super-linear relation with modulation phase $\Delta\varphi_{\mathrm{mod}}$ [red curve in (b)] while the intensity stays at unity level [blue curve in (b)]. (c) This super-linearity could be designed to compensate for the sub-linearity of the MZI at the quadrature point when the two arms combine, (d) therefore realizing a much-linearized Fano line shape in the full RAMZI device.

3. DEVICE FABRICATION AND CHARACTERIZATIONS

We fabricate the RAMZI modulators from commercially available 500-nm-thick *x*-cut LN thin films (NANOLN). Optical waveguide and resonator patterns are first defined in hydrogen silsesquioxane (HSQ) using electron-beam lithography (EBL, 50 keV) and are then transferred into the LN layer using optimized argon plasma-based reactive ion etching (RIE) [43]. The LN etch depth is ~250 nm, leaving a 250-nm-thick slab, which allows us to achieve a good balance between optical confinement and EO overlap within fabrication constraints [23,25,28]. The designed top widths of the optical waveguides and the racetrack resonator are both 1.2 µm to suppress excessive higher order optical modes. After removing the remaining resist, the devices are cladded in a 1.5-µm-thick SiO$_2$ layer using plasma-enhanced chemical vapor deposition (PECVD). Gold electrodes and probe contact pads are subsequently formed by aligned photolithography, electron-beam evaporation, and lift-off processes. The modulation electrodes are placed along the two straight sections of the racetrack resonator,

with a total effective modulation length of 2 mm per round trip. The positive and negative electrodes are spaced by a gap of 5 µm to ensure strong EO coupling while minimizing metal-induced optical losses. The final devices are cleaved for end-fire coupling. The measured insertion loss of the fabricated RAMZI modulator is 10.5 dB, including a 2.5 dB on-chip loss (2.2 dB from MMIs and 0.3 dB from propagation loss) and a total of 8 dB loss from fiber-to-chip coupling.

We show strongly linearized modulation transfer function in our fabricated RAMZI devices (Fig. 2). Across the measured spectrum, the device exhibits distinct line shapes depending on the phase difference between the two arms of the unbalanced MZI, $\Delta\varphi_{\mathrm{mzi}}$ [purple dashed line of Fig. 2(a)], including Lorentzian, Fano, and electromagnetically induced transparency (EIT)-like line shapes. This is a result of the interference between the narrowband racetrack resonator (FSR ~ 0.4 nm) and the broadband phase response of the unbalanced MZI (FSR ~ 20 nm) according to the Fano–Anderson model [44]. Linearized Fano line shape could be clearly observed at the quadrature points of the MZI ($\Delta\varphi_{\mathrm{mzi}} = \pi/2$ or $3\pi/2$),
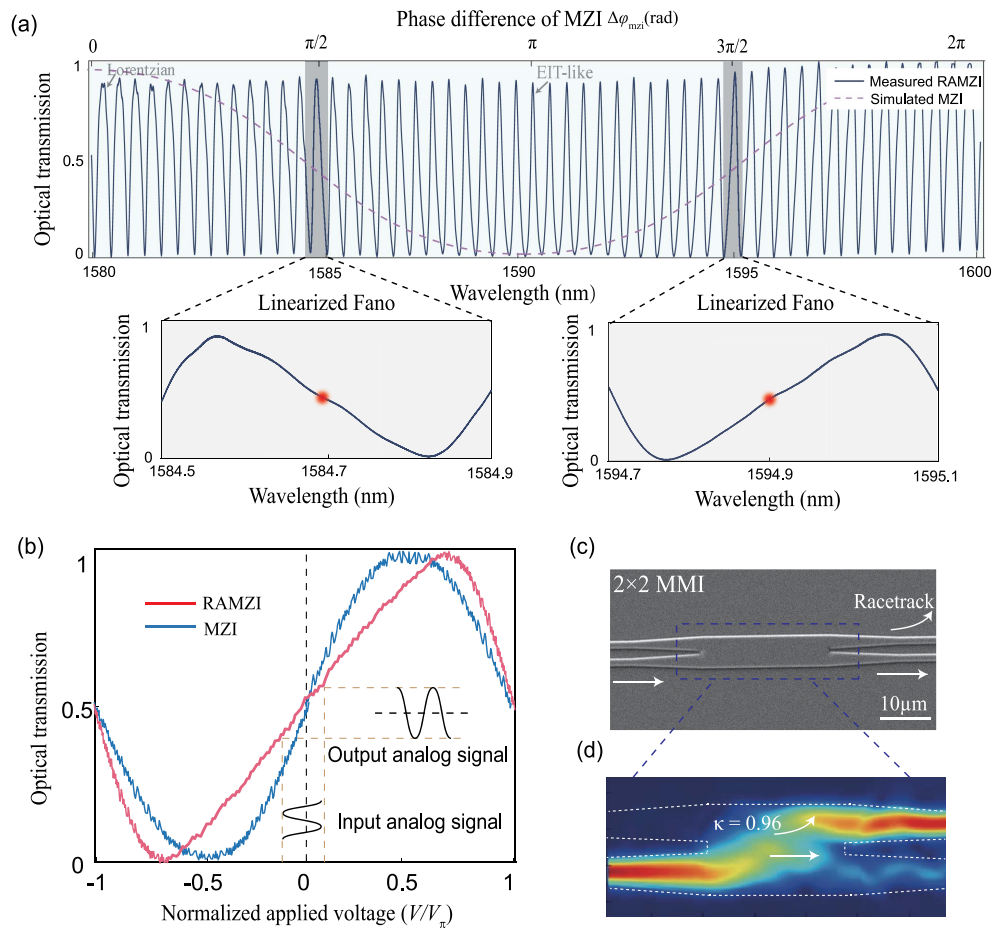
Fig. 2. Optical characterization of the RAMZI. (a) Measured optical transmission spectrum of the fabricated RAMZI device (blue solid curve), showing different line shapes depending on the phase difference $\Delta\varphi_{mzi}$ of the unbalanced MZI (purple dashed line). Linearized Fano line shape could be observed at the quadrature points of the MZI ($\Delta\varphi_{mzi} = \pi/2$ or $3\pi/2$), as shown in the insets. (b) Measured optical transmissions of the RAMZI modulator (red) and a reference MZI modulator (blue), as functions of applied voltages, showing a broadened linear regime in the RAMZI. The applied voltages are normalized by the respective half-wave voltages, V_π, for easier comparison. (c) SEM image of the 2 × 2 MMI structure used for achieving the deep overcoupling state of the racetrack resonator. (d) Simulated electric field intensity evolution along the 2 × 2 MMI structure with a coupling coefficient of $\kappa = 0.96$.

as shown in the insets of Fig. 2(a), which agrees well with the theoretical prediction in Fig. 1(d). We measure the EO transfer function of the RAMZI at this quadrature point by applying a 10 kHz triangular voltage signal, which could effectively avoid the impact from slow photorefractive-induced drifts when using direct current (DC), and monitoring the output optical signals [red curve of Fig. 2(b)]. As a side-by-side comparison, we also fabricate a reference MZI modulator on the same chip using similar waveguide dimensions and electrode design, the measured transfer function of which is plotted in the same figure (blue). The reference MZI features a modulation arm length of 5 mm, which does not substantially change the SFDR since a longer electrode leads to higher signal gain and IMD3 simultaneously. The applied voltages in Fig. 2(b) are normalized by the corresponding half-wave voltages (V_π) of the respective devices for better comparison (definition of V_π for RAMZI follows that defined in Ref. [31]). The voltage-length products ($V_\pi \cdot L$) are measured to be 3.8 V·cm

for the RAMZI modulator and 3.5 V·cm for the reference MZI modulator. The transfer function of the RAMZI modulator clearly shows a broadened linear regime compared with that of the reference MZI modulator. This indicates that the optimized design parameters, in particular the coupling ratio of the MMI, have been precisely achieved in the fabricated devices. Figure 2(c) shows the scanning electron microscope (SEM) image of the fabricated 2 × 2 MMI structure, which is designed to be broadband and fabrication-tolerant. Figure 2(d) shows the simulated electric field intensity evolution within the MMI structure for fundamental transverse-electric (TE) mode, transferring $|\kappa|^2 \sim 92\%$ of the optical power from the bus waveguide into the racetrack resonator (and vice versa) for each round trip. The measured coupling coefficient using a standalone MMI fabricated on the same chip agrees well with the designed value over a broad bandwidth from 1500 to 1630 nm, with a measured insertion loss of 0.8 dB. The measured 3 dB bandwidth of the RAMZI modulator is ~10 GHz, currently

limited by both the photon lifetime of the racetrack resonator (linewidth $\sim$ 17 GHz) and the resistance-capacitance (RC) constant of the lumped capacitor (RC limit $\sim$ 10 GHz). Traveling-wave electrodes could be adopted in the future to further increase the electrical bandwidth limit to beyond 100 GHz [23,25,28].

We demonstrate ultra-high SFDR values up to 120.04 dB · Hz$^{4/5}$ in our RAMZI modulator using the measurement setup shown in Fig. 3(a). In contrast to most integrated MWP demonstrations on other platforms [24,25, 34–36,40,41], our test link does not require an erbium-doped fiber amplifier (EDFA) after modulation due to the high-power handling capability of our LN devices, therefore minimizing the additional noise from EDFA when amplifying small signals. Specifically, a continuous-wave pump laser (Santec TSL510) at 1594.9 nm is amplified by an L-band EDFA (Amonics) and sent to the devices under test using a lensed fiber after a polarization controller to ensure TE polarization. The device could also operate in the telecom C-band given that the correct bias point is chosen and a C-band EDFA is used. The output optical signal is collected using a second lensed fiber and sent to either a 125 MHz photodetector (PD, New Focus 1811) for low-frequency measurements, or a 70 GHz PD (Finisar XPDV3120R) for high-frequency characterizations. Two sinusoidal RF signals separated by 10 MHz in frequency are generated using two microwave sources (R&S SMU200A, Hittite HMC-T2240) and injected into the modulation electrodes via a high-speed ground-signal (GS) probe (GGB Industries). The fundamental harmony (FH) and IMD3 components are then measured using an RF spectrum analyzer (R&S FSV7) at various input RF powers and frequencies. Figures 3(b) and 3(c) show the measured output FH and the IMD3 products as functions of the input RF powers for both the RAMZI modulator (red) and the reference MZI modulator (blue) at center signal frequencies of

1 GHz and 5 GHz, respectively. Notably, the IMD3 signals in our RAMZI show a slope of 5 in the log-log scale at both frequencies (red dashed lines), indicating that the cubic terms of IMD3 are strongly suppressed and now the fifth-order terms dominate. To the best of our knowledge, such strong suppression has not been achieved in RAMZI modulators in other material platforms [33–35] and is only made possible in a platform with an intrinsically linear material response and optimized RAMZI implementations. Since the leading spurious harmonics scale to the fifth power, the SFDR value now takes a unit of dB · Hz$^{4/5}$ when normalized with the resolution bandwidth of the noise floor. Considering the noise floor of −133.8 dBm at 1 GHz during our measurement under a resolution bandwidth of 1 kHz (equivalent to −163.8 dBm/Hz, limited by the RF spectrum analyzer), our RAMZI device shows an ultra-high SFDR of 120.04 dB · Hz$^{4/5}$ when the optical power reaches the saturation level of our PD [Fig. 3(b)]. The measured SFDR represents an 18 dB improvement over the reference MZI under the same measurement condition and a similar level of improvement over previous integrated LN demonstrations [24,25]. It should be noted that, since SFDR values may take different units (i.e., dB · Hz$^{4/5}$ for our RAMZI and dB · Hz$^{2/3}$ for MZI), they can only be compared at a certain resolution bandwidth. Here we adopt the most commonly used normalization of 1 Hz for comparison. The measured SFDR is also the highest value achieved in any integrated photonic platform without active feedback controls [24,25,34–36, 40,41]. At a frequency of 5 GHz (10% of the ring FSR), the measured SFDR drops to 114.54 dB · Hz$^{4/5}$ due to the bandwidth limitation of the resonator, yet it still represents a 13 dB improvement from the reference MZI modulator [Fig. 3(c)].

To further confirm that our RAMZI is indeed biased at the optimal operating points, we measure the FH and IMD3 signals at various detuning wavelengths within one FSR of the resonator, near two different quadrature points [i.e., $\Delta\varphi_{mzi} = \pi/2$ and $3\pi/2$ in Figs. 4(a) and 4(b), respectively]. Here the two input RF tones are fixed at a relatively high power of 15 dBm near 1 GHz, such that the IMD3 products can be reliably measured. At off-resonance points B and E, which also correspond to the detuning conditions used in Figs. 3(b) and 3(c), strong suppression of the IMD3 products could clearly be observed (red dashed lines), therefore giving rise to the highest carrier-to-distortion (FH/IMD3) ratio and in turn the highest SFDR [Figs. 4(a) and 4(b)]. In contrast, other detuning points, e.g., A, C, D, or E, exhibit lower SFDR values due to significantly higher IMD3 powers, despite their higher modulation efficiencies and FH signals [blue dashed lines in Figs. 4(a) and 4(b)].

We show that the high-power handling capability of our thin-film LN platform is a key enabler for the high SFDRs demonstrated. Figure 4(c) shows the measured SFDRs at various received optical powers via changing the EDFA gain when the device is kept at the optimal operation point. Since the noise floor in our measurements is limited by the RF spectrum analyzer and is not affected by the EDFA gain, increasing the optical power only elevates the FH and IMD3 products, leading to higher interception points between these tones and larger SFDRs. In our system where SFDR is limited by the fifth-order
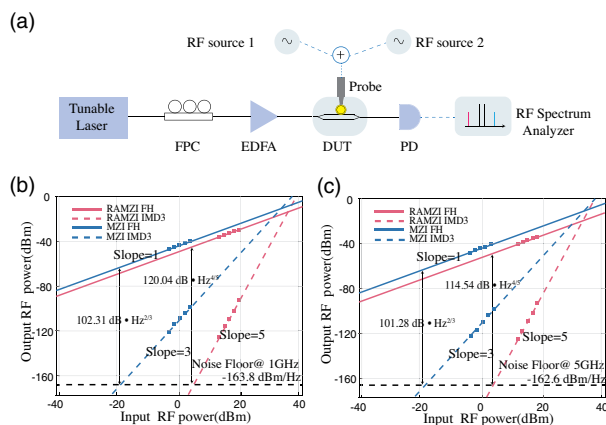

Fig. 3. Linearity performance of the RAMZI modulator. (a) Experimental setup for SFDR measurements. The test link does not require an EDFA after modulation due to the high-power handling capability of LN, therefore minimizing the extra noise from EDFA when amplifying small signals. FPC, fiber polarization controller; DUT, device under test. (b),(c) Measured output FH and IMD3 powers versus input RF powers for the RAMZI (red) and the reference MZI (blue), showing high SFDR values of 120.04 dB · Hz$^{4/5}$ and 114.54 dB · Hz$^{4/5}$ at 1 GHz (b) and 5 GHz (c), respectively.
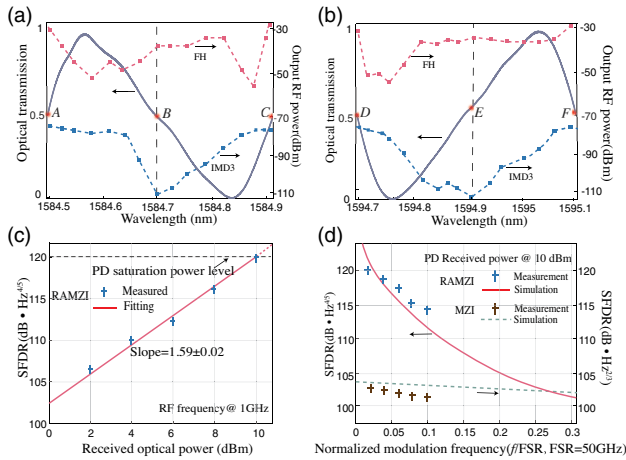
Fig. 4. Detuning and power dependence of the RAMZI modulator. (a), (b) Measured FH (red) and IMD3 (blue) powers at various detuning wavelengths within one FSR when the MZI is biased at (a) $\Delta\varphi_{mzi} = \pi/2$ and (b) $\Delta\varphi_{mzi} = 3\pi/2$, at a fixed input RF power of 15 dBm. Strong suppression of the IMD3 products could be observed at the off-resonance points (B and E). (c) Measured SFDRs at 1 GHz as a function of the received optical powers, with a fitted slope of 1.59 ± 0.02 in log-log scale. The highest SFDR is measured at a received power of 10 dBm, limited by the PD saturation power (black dash line). (d) Measured and simulated SFDRs at different RF frequencies (normalized by the resonator FSR) for the RAMZI and the reference MZI.

Fig. 5. Simulated SFDR values as functions of modulation frequency for RAMZIs with different FSRs (solid lines), as well as MZI (green dashed line). The 170 GHz RAMZI shows nearly 10 dB improvement over MZI even at a high frequency of 26 GHz, covering the entire microwave K band.

terms, a 1 dB increment in optical power gives rise to a 1.6 dB increase in SFDR value. This trend extends until the optical power reaches the PD saturation level [10 dBm, dashed line in Fig. 4(c)], which corresponds to an optical power of 125 mW on chip, without the need for an EDFA after the modulator. Considering the devices could possibly take even higher optical powers [12], we could in principle further increase the input power to compensate for any possible loss in the RF photonic link (e.g., a fiber link over many kilometers). A similar level of SFDR could, thus, be maintained even when the system exhibits a relatively high link loss, as long as the PD could still be saturated.

4. DISCUSSIONS AND OUTLOOK

The record-high SFDR of 120.04 dB $\cdot$ Hz$^{4/5}$ in our integrated LN RAMZI modulators, achieved without the need for active feedback controls, results from a combination of the intrinsically linear EO response of LN and the high-power handling capability of the thin-film LN platform, as well as optimized RAMZI design and implementation. Even higher SFDR could possibly be achieved in the future by using a PD with higher gain or saturation power, and/or adopting more advanced device configurations to cancel out the fifth-order terms of IMD3 [41]. Further implementing low-loss fiber-chip couplers [45–47] and increasing the optical powers could lead to long-distance radio-over-fiber links with high gain and high linearity simultaneously.

One limitation of the RAMZI scheme is that the SFDR value drops at higher RF frequencies due to the narrowband nature of the racetrack resonator, as our measurement and
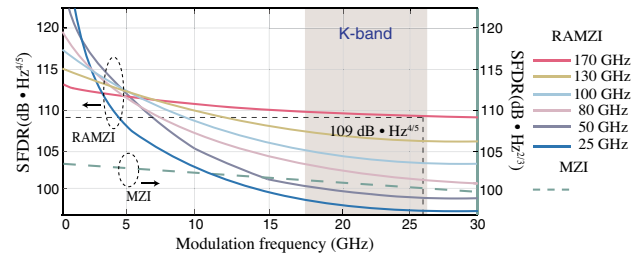
simulation results show in Fig. 4(d). The RAMZI modulator offers improved SFDR over the reference MZI modulator at modulation frequencies up to 27% of the FSR (13.5 GHz in this case) according to the simulation results. Larger linearized RF bandwidths could be achieved using smaller ring/racetrack resonators with larger FSRs, at the cost of decreased modulation efficiencies (due to shorter electrode lengths) and lowered link gain. Our simulation results shown in Fig. 5 suggest that, using a 170 GHz FSR microresonator, we could still reach a high SFDR value of 109 dB $\cdot$ Hz$^{4/5}$ even at a frequency of 26 GHz, which is nearly 10 dB better than that of an MZI and enough to cover the entire microwave K band. We note that, although SFDR is already a comprehensive system parameter that simultaneously captures the link gain, spurious harmonics, and noise floor, for certain application scenarios the absolute modulation efficiency could be important and should be designed together with the SFDR consideration. In such cases, the preferred FSR should be chosen to achieve a good balance among modulation efficiency, linearity, and the operation bandwidth (Fig. 5).

Importantly, our ultra-linear RAMZI modulators are highly compatible with other high-performance photonic components available on the integrated LN platform, both in terms of waveguide/electrode designs and fabrication processes. Further equipping these linearized modulators with an EO or thermo-optic phase shifter in one arm of the RAMZI could allow effective tuning of the working optical wavelength and active stabilization of the system bias point over possible drifts [28]. The high-linearity integrated modulators could become crucial elements for faithful transmission of advanced digital (e.g., pulsed-amplitude modulation, PAM-4/8) and analog signals in optical communication systems. Further integration of these linearized modulators with frequency comb sources, tunable filters, programmable switches, and low-loss delay lines could lead to chip-scale MWP systems with unique functionalities that are not currently achievable in other photonic platforms, enabling advanced MWP applications like broadband RF signal generation, radio-over-fiber links, and RF photonic signal processing.

REFERENCES

1. D. Marpaung, J. Yao, and J. Capmany, "Integrated microwave photonics," Nat. Photonics **13**, 80–90 (2019).
2. M. H. Khan, H. Shen, Y. Xuan, L. Zhao, S. Xiao, D. E. Leaird, A. M. Weiner, and M. Qi, "Ultrabroad-bandwidth arbitrary radiofrequency waveform generation with a silicon photonic chip-based spectral shaper," Nat. Photonics **4**, 117–122 (2010).
3. J. Wang, H. Shen, L. Fan, R. Wu, B. Niu, L. T. Varghese, Y. Xuan, D. E. Leaird, X. Wang, and F. Gan, "Reconfigurable radio-frequency arbitrary waveforms synthesized in a silicon photonic chip," Nat. Commun. **6**, 5957 (2015).
4. B. J. Eggleton, C. G. Poulton, P. T. Rakich, M. J. Steel, and G. Bahl, "Brillouin integrated photonics," Nat. Photonics **13**, 664–677 (2019).
5. C. G. Roeloffzen, L. Zhuang, C. Taddei, A. Leinse, R. G. Heideman, P. W. van Dijk, R. M. Oldenbeuving, D. A. Marpaung, M. Burla, and K.-J. Boller, "Silicon nitride microwave photonic circuits," Opt. Express **21**, 22937–22961 (2013).
6. J. S. Fandiño, P. Muñoz, D. Doménech, and J. Capmany, "A monolithic integrated photonic microwave filter," Nat. Photonics **11**, 124–129 (2017).
7. W. Liu, M. Li, R. S. Guzzon, E. J. Norberg, J. S. Parker, M. Lu, L. A. Coldren, and J. Yao, "A fully reconfigurable photonic integrated signal processor," Nat. Photonics **10**, 190–195 (2016).
8. V. J. Urick, K. J. Williams, and J. D. McKinney, *Fundamentals of Microwave Photonics* (Wiley, 2015).
9. D. Zhu, L. Shao, M. Yu, R. Cheng, B. Desiatov, C. Xin, Y. Hu, J. Holzgrafe, S. Ghosh, and A. Shams-Ansari, "Integrated photonics on thin-film lithium niobate," Adv. Opt. Photon. **13**, 242–352 (2021).
10. A. Karim and J. Devenport, "Noise figure reduction in externally modulated analog fiber-optic links," IEEE Photon. Technol. Lett. **19**, 312–314 (2007).
11. P. A. Morton, J. B. Khurgin, and M. J. Morton, "All-optical linearized Mach-Zehnder modulator," Opt. Express **29**, 37302–37313 (2021).
12. C. Wang, M. Zhang, M. Yu, R. Zhu, H. Hu, and M. Loncar, "Monolithic lithium niobate photonic circuits for Kerr frequency comb generation and modulation," Nat. Commun. **10**, 978 (2019).
13. M. Zhang, B. Buscaino, C. Wang, A. Shams-Ansari, C. Reimer, R. Zhu, J. M. Kahn, and M. Lončar, "Broadband electro-optic frequency comb generation in a lithium niobate microring resonator," Nature **568**, 373–377 (2019).
14. Z. Gong, X. Liu, Y. Xu, and H. X. Tang, "Near-octave lithium niobate soliton microcomb," Optica **7**, 1275–1278 (2020).
15. Y. He, J. Ling, M. Li, and Q. Lin, "Perfect soliton crystals on demand," Laser Photon. Rev. **14**, 1900339 (2020).
16. R. Gao, N. Yao, J. Guan, L. Deng, J. Lin, M. Wang, L. Qiao, W. Fang, and Y. Cheng, "Lithium niobate microring with ultra-high Q factor above 10⁸," Chin. Opt. Lett. **20**, 011902 (2022).
17. M. Zhang, C. Wang, R. Cheng, A. Shams-Ansari, and M. Lončar, "Monolithic ultra-high-Q lithium niobate microring resonator," Optica **4**, 1536–1537 (2017).

18. M. R. Escalé, D. Pohl, A. Sergeyev, and R. Grange, "Extreme electro-optic tuning of Bragg mirrors integrated in lithium niobate nanowaveguides," Opt. Lett. **43**, 1515–1518 (2018).
19. Y. Hu, M. Yu, D. Zhu, N. Sinclair, A. Shams-Ansari, L. Shao, J. Holzgrafe, E. Puma, M. Zhang, and M. Lončar, "On-chip electro-optic frequency shifters and beam splitters," Nature **599**, 587–593 (2021).
20. J.-Y. Chen, Z.-H. Ma, Y. M. Sua, Z. Li, C. Tang, and Y.-P. Huang, "Ultra-efficient frequency conversion in quasi-phase-matched lithium niobate microrings," Optica **6**, 1244–1245 (2019).
21. J. Lu, J. B. Surya, X. Liu, A. W. Bruch, Z. Gong, Y. Xu, and H. X. Tang, "Periodically poled thin-film lithium niobate microring resonators with a second-harmonic generation efficiency of 250,000%/W," Optica **6**, 1455–1460 (2019).
22. J.-X. Zhou, R.-H. Gao, J. Lin, M. Wang, W. Chu, W.-B. Li, D.-F. Yin, L. Deng, Z.-W. Fang, and J.-H. Zhang, "Electro-optically switchable optical true delay lines of meter-scale lengths fabricated on lithium niobate on insulator using photolithography assisted chemo-mechanical etching," Chin. Phys. Lett. **37**, 084201 (2020).
23. C. Wang, M. Zhang, X. Chen, M. Bertrand, A. Shams-Ansari, S. Chandrasekhar, P. Winzer, and M. Lončar, "Integrated lithium niobate electro-optic modulators operating at CMOS-compatible voltages," Nature **562**, 101–104 (2018).
24. A. Rao, A. Patil, P. Rabiei, A. Honardoost, R. DeSalvo, A. Paolella, and S. Fathpour, "High-performance and linear thin-film lithium niobate Mach–Zehnder modulators on silicon up to 50 GHz," Opt. Lett. **41**, 5700–5703 (2016).
25. M. He, M. Xu, Y. Ren, J. Jian, Z. Ruan, Y. Xu, S. Gao, S. Sun, X. Wen, and L. Zhou, "High-performance hybrid silicon and lithium niobate Mach–Zehnder modulators for 100 Gbit s⁻¹ and beyond," Nat. Photonics **13**, 359–364 (2019).
26. P. Kharel, C. Reimer, K. Luke, L. He, and M. Zhang, "Breaking voltage–bandwidth limits in integrated lithium niobate modulators using micro-structured electrodes," Optica **8**, 357–363 (2021).
27. A. J. Mercante, S. Shi, P. Yao, L. Xie, R. M. Weikle, and D. W. Prather, "Thin film lithium niobate electro-optic modulator with terahertz operating bandwidth," Opt. Express **26**, 14810–14816 (2018).
28. M. Xu, M. He, H. Zhang, J. Jian, Y. Pan, X. Liu, L. Chen, X. Meng, H. Chen, and Z. Li, "High-performance coherent optical modulators based on thin-film lithium niobate platform," Nat. Commun. **11**, 3911 (2020).
29. P. O. Weigel, J. Zhao, K. Fang, H. Al-Rubaye, D. Trotter, D. Hood, J. Mudrick, C. Dallo, A. T. Pomerene, and A. L. Starbuck, "Bonded thin film lithium niobate modulator on a silicon photonics platform exceeding 100 GHz 3-dB electrical modulation bandwidth," Opt. Express **26**, 23728–23739 (2018).
30. X. Xie, J. Khurgin, J. Kang, and F.-S. Chow, "Linearized Mach-Zehnder intensity modulator," IEEE Photon. Technol. Lett. **15**, 531–533 (2003).
31. H. Tazawa and W. H. Steier, "Bandwidth of linearized ring resonator assisted Mach-Zehnder modulator," IEEE Photon. Technol. Lett. **17**, 1851–1853 (2005).
32. J. Yang, F. Wang, X. Jiang, H. Qu, M. Wang, and Y. Wang, "Influence of loss on linearity of microring-assisted Mach-Zehnder modulator," Opt. Express **12**, 4178–4188 (2004).
33. S. Chen, G. Zhou, L. Zhou, L. Lu, and J. Chen, "High-linearity Fano resonance modulator using a microring-assisted Mach–Zehnder structure," J. Lightwave Technol. **38**, 3395–3403 (2020).
34. C. Zhang, P. A. Morton, J. B. Khurgin, J. D. Peters, and J. E. Bowers, "Ultralinear heterogeneously integrated ring-assisted Mach–Zehnder interferometer modulator on silicon," Optica **3**, 1483–1488 (2016).
35. J. Cardenas, P. A. Morton, J. B. Khurgin, A. Griffith, C. B. Poitras, K. Preston, and M. Lipson, "Linearized silicon modulator based on a ring assisted Mach Zehnder inteferometer," Opt. Express **21**, 22549–22557 (2013).
36. M. Streshinsky, A. Ayazi, Z. Xuan, A. E.-J. Lim, G.-Q. Lo, T. Baehr-Jones, and M. Hochberg, "Highly linear silicon traveling wave Mach-Zehnder carrier depletion modulator based on differential drive," Opt. Express **21**, 3818–3825 (2013).

37. A. Ayazi, T. Baehr-Jones, Y. Liu, A. E.-J. Lim, and M. Hochberg, "Linearity of silicon ring modulators for analog optical links," Opt. Express **20**, 13115–13122 (2012).

38. C. Manolatou and M. Lipson, "All-optical silicon modulators based on carrier injection by two-photon absorption," J. Lightwave Technol. **24**, 1433–1439 (2006).

39. D. A. Miller, D. Chemla, T. Damen, A. Gossard, W. Wiegmann, T. Wood, and C. Burrus, "Band-edge electroabsorption in quantum well structures: the quantum-confined Stark effect," Phys. Rev. Lett. **53**, 2173–2176 (1984).

40. Q. Zhang, H. Yu, L. Wang, P. Xia, Q. Cheng, Z. Fu, X. Wang, and J. Yang, "Silicon dual-series Mach–Zehnder modulator with high linearity," Opt. Lett. **44**, 5655–5658 (2019).

41. Q. Zhang, H. Yu, P. Xia, Z. Fu, X. Wang, and J. Yang, "High linearity silicon modulator capable of actively compensating input distortion," Opt. Lett. **45**, 3785–3788 (2020).

42. Q. Zhang, H. Yu, H. Jin, T. Qi, Y. Li, J. Yang, and X. Jiang, "Linearity comparison of silicon carrier-depletion-based single, dual-parallel, and dual-series Mach–Zehnder modulators," J. Lightwave Technol. **36**, 3318–3331 (2018).

43. K. Zhang, Z. Chen, H. Feng, W.-H. Wong, E. Y.-B. Pun, and C. Wang, "High-*Q* lithium niobate microring resonators using lift-off metallic masks," Chin. Opt. Lett. **19**, 060010 (2021).

44. L. Gu, L. Fang, H. Fang, J. Li, J. Zheng, J. Zhao, Q. Zhao, and X. Gan, "Fano resonance lineshapes in a waveguide-microring structure enabled by an air-hole," APL Photon. **5**, 016108 (2020).

45. C. Hu, A. Pan, T. Li, X. Wang, Y. Liu, S. Tao, C. Zeng, and J. Xia, "High-efficient coupler for thin-film lithium niobate waveguide devices," Opt. Express **29**, 5397–5406 (2021).

46. P. Ying, H. Tan, J. Zhang, M. He, M. Xu, X. Liu, R. Ge, Y. Zhu, C. Liu, and X. Cai, "Low-loss edge-coupling thin-film lithium niobate modulator with an efficient phase shifter," Opt. Lett. **46**, 1478–1481 (2021).

47. L. He, M. Zhang, A. Shams-Ansari, R. Zhu, C. Wang, and L. Marko, "Low-loss fiber-to-chip interface for lithium niobate photonic integrated circuits," Opt. Lett. **44**, 2314–2317 (2019).